HAL
open science

Dual-layer catalyst layers for increased proton exchange membrane fuel cell performance

Yannick Garsany, Robert Atkinson, Benjamin Gould, Rachel Martin, Laetitia Dubau, Marian Chatenet, Karen Swider-Lyons

To cite this version:

Yannick Garsany, Robert Atkinson, Benjamin Gould, Rachel Martin, Laetitia Dubau, et al.. Dual-layer catalyst layers for increased proton exchange membrane fuel cell performance. Journal of Power Sources, 2021, 514, pp.230574. 10.1016/j.jpowsour.2021.230574 . hal-03453395

HAL Id: hal-03453395

https://hal.science/hal-03453395v1

Submitted on 9 Dec 2022

HAL is a multi-disciplinary open access archive for the deposit and dissemination of scientific research documents, whether they are published or not. The documents may come from teaching and research institutions in France or abroad, or from public or private research centers.

L'archive ouverte pluridisciplinaire **HAL**, est destinée au dépôt et à la diffusion de documents scientifiques de niveau recherche, publiés ou non, émanant des établissements d'enseignement et de recherche français ou étrangers, des laboratoires publics ou privés.

Dual-Layer Catalyst Layers for Increased Proton Exchange Membrane Fuel Cell Performance

Yannick Garsany[a#], Robert W. Atkinson III[a], Benjamin D. Gould[b], Rachel Martin[c], Laetitia Dubau[d], Marian Chatenet[d], and Karen E. Swider-Lyons[b]

[a]Excet Inc., Springfield, VA 22151

[b]Chemistry Division, Code 6173, U.S. Naval Research Laboratory, Washington, DC 20375

[c]Univ. Grenoble Alpes, Univ. Savoie Mont Blanc, CNRS, Grenoble INP*, CMTC, 38000 Grenoble, France

[d]Univ. Grenoble Alpes, Univ. Savoie Mont Blanc, CNRS, Grenoble INP*, LEPMI, 38000 Grenoble, France

*Institute of Engineering and Management Univ. Grenoble Alpes

[#]Corresponding author: yannick.garsany.ctr@nrl.navy.mil

Abstract

The use of a dual-layer cathode catalyst layer improves the performance of proton exchange membrane fuel cells. To generate single and dual-layer catalyst layers between the gas diffusion media and proton exchange membrane electrolyte, two commercial carbon-supported platinum catalysts with either a high microporosity carbon (Ketjen Black EC-300J) or a low porosity carbon (XC-72 Vulcan carbon) are utilized. We discovered that dual-layer cathode catalyst layers boost maximum power of fuel cells regardless of carbon porosity directionality, with either high surface area carbon at the proton exchange membrane electrolyte or gas diffusion media interface. At 25% relative humidity, a condition that generally inhibits

fuel cell performance, a 20% performance boost is realized when using dual-layer cathode CLs. The electrochemical impedance spectroscopy results indicate that cathodes with dual-layer catalyst layer aid in water management due to lower kinetic activity losses of the Pt and improved hydration of the proton exchange membrane electrolyte.

1. Introduction

The optimization of the catalyst layers (CLs) is critical for high proton exchange membrane fuel cell (PEMFC) performance, especially the cathode CL, which is where the oxygen reduction reaction (ORR) occurs [1, 2]:

$$O_2 + 4H^+ + 4e^- \leftrightarrow 2H_2O \qquad [1]$$

The CL must have suitable porosity and ionomer coverage for effective proton (H^+), gas, and water transport for operation at high current density, in addition to having an active catalyst for good kinetics. [3]. The CL's pore structure must offer adequate paths for O_2 to reach the cathode while also allowing for the clearance of remaining liquid water that could flood the electrodes and obstruct mass transport. A typical cathode CL comprises platinum-based nanoparticles supported on porous carbon microparticles that are connected through a continuous H^+-conducting ionomer network. The CL connects with the H^+-conducting polymer electrolyte membrane (PEM) on one side, and the other side contacts gas diffusion media (GDM), which manages gas and water transport to and from the CL. More information on how a fuel cell or a membrane electrode assembly (MEA) is built can be found elsewhere [4].

An ideal CL will have low charge-transport resistance for the ORR, low mass-transport resistance for O_2, and low ionic resistance in the ionomer of the CL, in particular at low relative humidity (not to mention low ionic resistance required for the PEM). Researchers have attempted to meet these attributes through the optimization of the ionomer content [5-7] and ionomer type [2, 8-12] for improved H^+ conductivity, and the introduction of pore formers [13, 14] or the optimization of the carbon substrate morphology [15-17], for better mass transport of gas and water. Such properties are sought with modifications of the ink formulations [18, 19] and the methods used to deposit the CLs [10, 20-22].

Others have studied the impact of materials gradients in the plane of the CL, owing to the expected change in concentration of the reactants/products concentration along the length of the feeding channel [23, 24]. Because the concentrations of gas and water in the CLs are not uniform, and water concentration increases from the gas diffusion medium (GDM) to the PEM as reactants are consumed and products are generated, out-of-plane gradients of the CLs were also investigated. As a result, CLs with ionomer and Pt gradients have been created in order to reduce mass-transport losses and improve Pt utilization in cathode CLs. [25-43].

Many investigations have shown that ionomer gradients improve PEMFC performance when the ionomer content is higher toward the CL/PEM interface and lower toward the CL/GDM interface. [27, 32, 39, 43]. Higher ionomer content near the CL/PEM interface is expected to improve H^+ conductivity whereas lower ionomer content at the interface of the CL/GDM should increase the CL porosity and improve gas transport and water removal. The impact of grading the Pt loading in PEMFC CL has been studied in through-plane [29, 30, 33, 35, 40] and in-plane configurations [26, 28, 31]. In through-plane grading, the Pt loading is graded through the thickness of the CL in the Z-direction and various investigations have demonstrated that a higher Pt loading near the CL/PEM interface maximizes the cell performance [30, 33, 35]. In in-plane grading CL, the Pt loading is graded along the length of the gas channel (the X-Y plane), and several studies have shown that increasing the Pt loading from the cathode inlet to the outlet also maximizes the cell performance [26, 28, 31] and can to minimize operation heterogeneities over the CL surface [24].

A tool that has not been explored for CL improvements (at least to the authors' knowledge) is gradients in porosity. Small pores (e.g. micropores, d <2 nm, or small mesopores, 2 nm < d< 50 nm) are crucial in water management, according to porosity models, since they increase water evaporation to the gas phase and heat transfer [44, 45]. We have reported that increasing the amount of small pores in the cathode CL increases the power production of the PEMFCs [2]. Based on our prior work, we can speculate that CLs

with non-uniform porosity through the thickness direction (i.e. the Z-direction) will improve water management and PEMFC power compared to conventional cathode CLs with homogenous porosity. A region of low extent of small pores should encourage liquid water retention for higher ionic conductivity, while high extent of small pores should encourage water evaporation for better mass-transport. Such water management is crucial for operating at low relative humidity, which is desired to avoid the requirement for external humidification, and high power, when there is significant water production.

To ascertain the impact of porosity gradients in CLs, we use an ultrasonic spray deposition (USD) [4, 46] to prepare dual-layer CLs with the average pore size either increasing or decreasing down the Z-direction, from the PEM to the GDM. The porosity gradients are created by using two types of carbon black Pt supported catalysts: Ketjen Black EC-300J supported Pt catalyst (Pt/KB) or XC-72 Vulcan carbon supported Pt catalyst (Pt/VC). Ketjen Black carbon support has a larger surface area, with average pore size of 34 nm and surface area of $\sim$ 800 m^2/g (before the addition of ionomer and formation into a CL). The surface area of XC-72 Vulcan carbon support is $\sim$ 218 m^2/g with a greater starting average pore size of 50 nm. Furthermore, when compared to XC-72 Vulcan carbon support, Ketjen Black carbon support has a higher percentage of micropores (i.e. 15% of the total pore volume vs. 25% of the total pore volume) [47, 48]. The resulting dual-layer catalyst layer structures are compared to baseline homogeneous single layer CL structures as well as a homogeneous catalyst layer that combines the two Pt/Carbon catalysts.

As described elsewhere, the platinum loadings in the dual-layer CLs were previously optimized to 0.19 mg_{Pt} cm^{-2} for the Pt/KB CL and 0.06 mg_{Pt} cm^{-2} for the Pt/VC CL [49], for a total Pt loading of 0.25 mg_{Pt} cm^{-2} in the cathode. We have also tested CLs with more than two layers and found the dual-layer CLs superior, so we focus on those results in this paper. Scanning electron microscopy (SEM) and N_2 physisorption studies are used to characterize the physical properties of the CLs. Electrochemical performance is measured for the single cells with polarization, or I-V curves at 25% and 100% relative humidity (RH). Electrochemical impedance spectroscopy (EIS) was measured at an operating cell voltage

of 0.60 V, where water production is strong and the roles of small pores are more important. The EIS analysis distinguishes the factors that contribute to PEMFC performance losses, such as ohmic resistance, charge-transfer resistance, and mass-transport resistance.

2. Experimental

2.1. Catalyst inks preparation and Catalyst Coated Membrane (CCM) manufacture.

The cathode CLs were made using a XC-72 Vulcan carbon supported Pt catalyst (Pt/VC, Hi-spec 4000, Johnson Matthey (JM), 40 wt. % Pt) or a Ketjen Black EC-300J supported Pt catalyst (Fuel Cell Store, 40 wt. %Pt). The Pt/Carbon catalyst were mixed with a 6wt. % Aquivion® ionomer aqueous solution (Aquivion® D83-06A, 830EW). The Aquivion® ionomer to carbon black mass ratio (I/C) was set to 0.62/1.

The anode CLs were made by mixing a carbon-black supported Pt catalyst (Pt/CB (TEC10E50E), Tanaka Kikinzoku Kogyo (TKK), 47.6 wt.% Pt) with a 15wt. % Nafion® ionomer solution in a homogenous manner (Liquion™ solution LQ1115, 1100EW). The Nafion® ionomer binder to carbon black mass ratio (I/C) was set to 0.95/1.

Using an automated ultrasonic spray coater, the cathode and anode CLs were directly deposited on top the Nafion® HP PEM [4, 46]. Further information on exact ink formulations and spraying parameters can be found in the Supporting Information (SI). Five sets of CCMs with distinctive cathode CL designs were fabricated as schematically depicted in Figure 1. The total Pt loading of the cathode CLs was set to ~0.25 mg_{Pt} cm^{-2}, and that of the anode CLs was set to ~0.14 mg_{Pt} cm^{-2}. The active geometric area of the anode and cathode CLs were 10 cm^2 (3.16 cm × 3.16 cm).

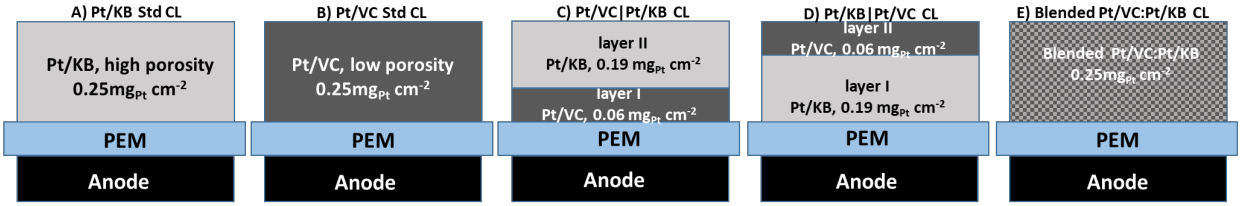

Figure 1. Illustrations of the five different cathode catalyst layers used in this study.

The standard (Std) high porosity or low porosity cathode CLs each had a single, homogenous layer of either Pt/KB or Pt/VC catalyst, respectively (Fig. 1A & 1B). The dual-layer CL CCMs (Fig. 1C) were prepared by spraying two distinctive layers: The first layer (i.e.layer I) was sprayed directly onto the HP Nafion® PEM and the second layer (i.e. layer II) was sprayed on top of layer I (i.e. on the GDM side). The Pt/VC|Pt/KB describes a CL with decreasing porosity along the Z-axis, or low porosity at the PEM interface. Layer I was fabricated by spraying the Pt/VC catalyst ink directly onto the Nafion® HP PEM yielding a CL with Pt loading of 0.06 mg$_{Pt}$ cm^{-2}. After overnight drying, layer II was fabricated by spraying the Pt/KB ink directly on top of layer I, resulting in a CL with a Pt loading of 0.19 mg$_{Pt}$ cm^{-2}. A dual-layer cathode with the opposite porosity gradient, Pt/KB|Pt/VC cathode CL CCM (Fig. 1D) was fabricated to understand the impact of high porosity at the PEM interface. In this case, layer I was fabricated by spraying the Pt/KB catalyst ink directly onto the Nafion® HP PEM, yielding a layer I with a Pt loading of 0.19 mg$_{Pt}$ cm^{-2}. Layer II was formed by spraying the Pt/VC ink straight on top of layer I after it had dried overnight, yielding a layer II with a Pt loading of 0.06 mg$_{Pt}$ cm^{-2}. The final cathode CL (Fig. 1E) was a homogenous cathode CL design comprising a 2:6 (wt.) blend of Pt/VC|Pt/KB ink sprayed directly onto the Nafion® HP PEM. Table S1 summarizes the properties of the prepared CCMs for PEMFCs testing.

2.2. Scanning Electron Microscopy (SEM)

A Field-emission-gun scanning electron microscopy (FEG-SEM, Zeiss Gemini 500 microscope) was used to acquire the scanning electron microscopy (SEM) images. The secondary electron detector (In lens detector) is positioned within the lens of this microscope together with a backscattered electron detector,

and it was developed to image electrons at low accelerating voltage (usually at or below 15 kV), which is required for polymer-containing materials such as PEMFC CCMs. Here, an acceleration voltage comprised between 3 and 15 kV was used, which enables to maximize the image resolution. The samples consisted of square zones cut in the above-mentioned CCMs, observed as cross-sections. CCM cross section samples were prepared by first embedding the CCMs in Epoxy® resin, drying them in ambient air for one day, polishing them with a SiC polishing disk with a small grain size (4000), and finally covering them with a thin carbon film.

2.3. Nitrogen-sorption porosimetry.

A Micromeritics ASAP 2010 N_2-sorption porosimeter was used for porosity analysis. Half-CCMs (i.e. only the cathode CL of interest deposited onto the Nafion® HP PEM) were prepared for these measurements. Prior to physiorption measurements, the manufactured CCMs were sliced into tiny strips and placed inside the porosimeter tube for degassing under vacuum at 100°C for 12 hours. The Brunauer-Emmett-Teller (BET) method was used to calculate the specific surface area and pore volume distribution (PSD). The BET surface area was calculated using the adsorption branch of the isotherm. The total pore volume was calculated at 0.98P/P0, the pore-size distribution (PSD) was calculated using the Barrett-Joyner-Halenda (BJH) model fitted to the Harkins Jura equation, and the micropore surface area was calculated using t-plot analysis [46, 50].

2.4. Membrane Electrode Assembly (MEA) and Testing.

Fuel cell tests were conducted in 10 cm^2 single cell hardware comprises of mirror single serpentine flow field for the anode and the cathode (Fuel Cell Technologies). We selected an asymmetrical GDM pairing with Freudenberg H24C3 on the anode and Freudenberg H23C2 on the cathode [51]. Virgin PTFE Skived Tape (Enflo) of different thicknesses are placed on the anode and cathode side of the HP Nafion® PEM to

the enable the desired compression. The target GDM compression was 28% as described in our previous publication [52, 53].

The performance of single cells was tested using Scribner 850e fuel cell test devices from Scribner Associates, Inc.. Experiments were conducted at a cell temperature of 80°C, and ambient pressure. The inlet dew point for both gases is fixed at 79.0°C or 49.2°C, corresponding to 100%, or 25% inlet relative humidity (RH). Ultrapure gases H_2 (HY UHP 300) or air (UZ 300) from Air-Liquide were supplied to the anode and cathode under stoichiometric flow conditions of 2/2 for H_2/air. All studies began with the MEA being broken in for 2 hours by maintaining the cell voltage at 0.60 V in H_2/air, followed by 20 cycles alternating between 0.70 V and 0.40 V for 10 minutes at a time.. I-V polarization curves were recorded at increments of 25 mV from open circuit voltage (OCV) to 0.20 V with hold times of 1 min/point. The standard deviation for three individual measurements on unique PEMFCs is represented by the error bars in the I-V polarization and power density curves.

Electrochemical impedance spectroscopy (EIS) was performed using the Scribner 850e fuel cell test system equipped with load and frequency analyzer [10]. Three successive EIS measurements were performed at the operating cell voltage of 0.60 V in H_2/air at 100%RH and 25%RH in potentiostatic mode to assess effective charge-transfer resistances and mass-transport restrictions. A 5-minute constant cell voltage hold preceded and followed each measurement. The measurements were carried out under the identical cell conditions as the performance test, including the same temperature, anode and cathode humidification temperatures. The EIS frequency range was from 10,000 to 0.1 Hz following a 5-minute hold at the selected cell voltage with an AC perturbation equal to 2% of the DC current. The exact experimental details for the fuel cell diagnostic measurements can be found in the SI.

3. Results and Discussion

3.1. Catalyst Layer Microstructure

Figure 2 depicts the cross-sectional SEM images of the five distinct cathode CLs at 5000x magnification in backscattered mode. These SEM images reveal that all the cathode CLs are uniformly deposited directly on the Nafion® HP PEM. The Pt/KB Std CL (Fig. 2A) appears to be thicker than the Pt/VC Std CL (Fig. 2B), presumably because of its higher porosity and surface area. The Pt/VC Std CL image appears brighter, indicative of a greater proportion of Pt nanoparticles on the surface of the support, as opposed to confined in internal voids of the KB carbon support particles [54, 55]. Platinum nanoparticles appear as bright spots and are equally and finely scattered throughout the Pt/KB Std CL; some larger Pt nanoparticle agglomerates are locally witnessed in the case of the Pt/VC Std CL. The duller SEM image for the Pt/KB Std CL indicates that the Pt nanoparticles are inside the pores and probably spread in the CL volume with less extent of agglomeration than for the Pt/VC Std CL. Despite looking denser than the Pt/KB Std CL, the Pt/VC Std CL appears to have more visible pores at this magnification.

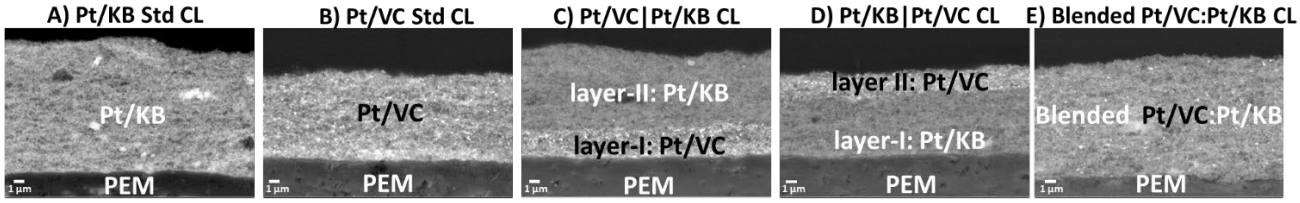

Figure 2. Cross-sectional scanning electron micrographs in backscattered mode of A) Pt/KB Std CL, B) Pt/VC Std CL, C) Pt/VC|Pt/KB CL, D) Pt/KB|Pt/VC CL and E) Blended Pt/VC:Pt/KB CL. Magnified 5000x.

In the dual-layer CLs, Pt/VC|Pt/KB and Pt/KB|Pt/VC (Fig. 2C & 2D), each respective layer appears to be uniform and well connected, with no presence of delamination or gap at any of the interfaces. The individual appearance/morphology of a single layer in the dual-layer CLs is comparable to the pure Pt/KB Std and Pt/VC Std CLs of Fig. 2A and Fig. 2B, respectively. In the Blended Pt/VC:Pt/KB CL (Fig. 2E), a uniform CL is observed, with very high porosity, suggesting very good mixing and distribution of the Pt/VC and

Pt/KB catalysts. Compared to Fig. 2B, the Pt/VC catalyst (bright spots) in the Blended Pt/VC:Pt/KB CL appear to be diluted throughout the CL and homogeneously distributed

The thicknesses of the prepared CLs were estimated using the SEM images in Fig. 2. As reported by Soboleva *et al*. [56], we observed that for identical Pt, ionomer, and carbon loading, the Pt/KB Std CL is slightly thicker (i.e. 10.2 µm) than the Pt/VC Std CL (i.e. 7.8 µm), indicating a less dense CL with a greater void space into which water can be assimilated. For the Pt/VC|Pt/KB CL, the thickness of the Pt/VC layer-I is 1.9 µm and that of the Pt/KB layer-II is 8.9 µm for a total thickness of 10.8 µm. For the Pt/KB|Pt/VC CL, the thickness of the Pt/KB layer-I is 8.2 µm and that of the Pt/VC layer-II is 2.6 µm for a total thickness of 10.8 µm. Finally, the thickness of the homogeneous Blended Pt/VC:Pt/KB CL is 10.4 µm.

3.2. Catalyst Layer Porosimetry

N_2 adsorption isotherms of the five CLs are shown in Figure 3A. All of the cathode CLs exhibit a Type II isotherm, with rapid N_2 adsorption in the macropore region, indicating that these CLs have a predominantly mesoporous structure. The Pt/KB Std CL (black curve) exhibits the largest amount of N_2 adsorbed and the Pt/VC Std CL (red curve) the smallest amount of N_2 adsorbed. The shape of the isotherm and the amount of N_2 adsorbed show the same pattern for the Pt/VC|Pt/KB CL, Pt/KB|Pt/VC CL and Blended Pt/VC:Pt/KB CL, matching expectation as all have the same stoichiometric amounts of the respective components. The adsorption isotherms for all CLs reveal a hysteresis loop, however the hysteresis is more pronounced for the Pt/KB Std CL, the Pt/VC|Pt/KB CL, Pt/KB|Pt/VC CL and Blended Pt/VC:Pt/KB CL over a wide range of the partial pressures down to 0.45 P/Po compared to the Pt/VC Std CL (i.e. at pressure above 0.80 P/Po). Similar results were obtained for CLs prepared using the decal transfer methodology with a Pt/KB and Pt/VC catalyst by Soboleva *et al.* [50]. The presence of mesopores in the CLs is shown by the hysteresis loop characteristic of capillary condensation at high pressure [57, 58].

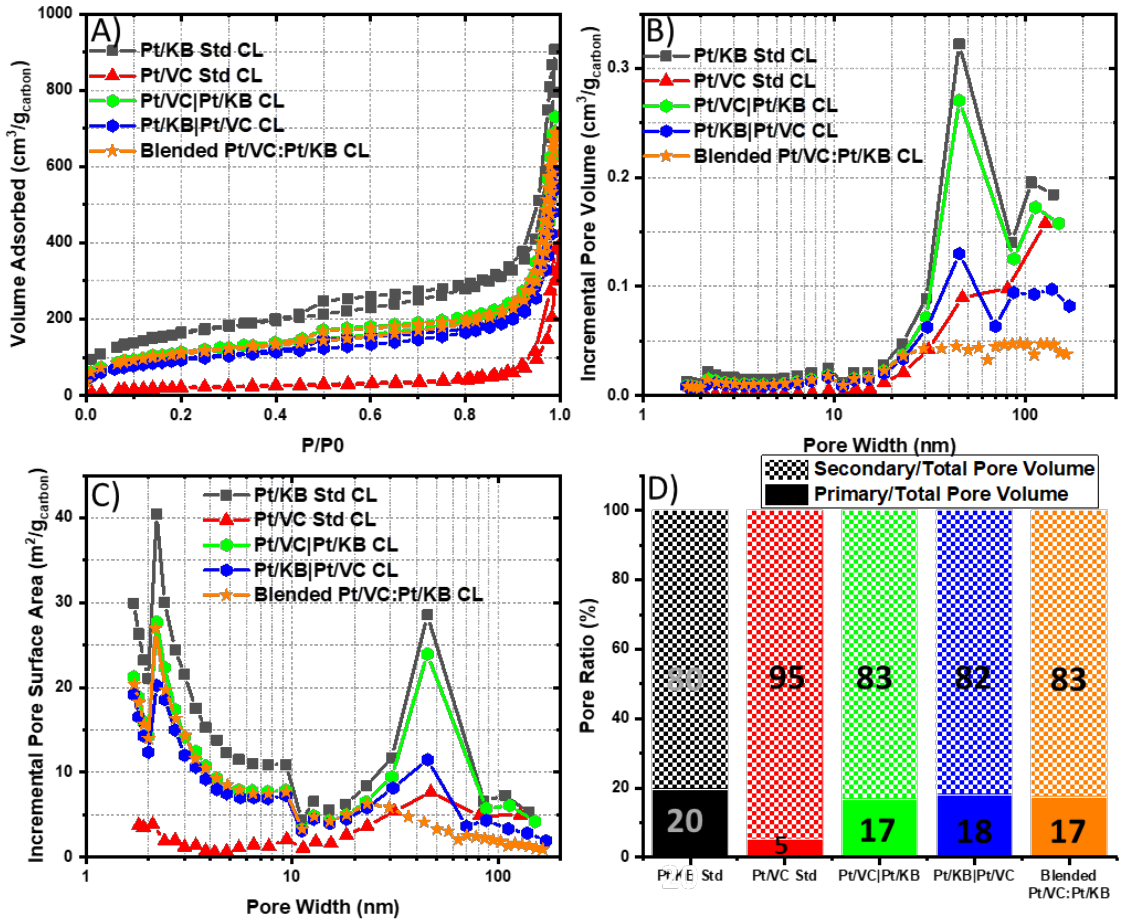

Figure 3. A) N_2-adsorption isotherms, B) Incremental Pore Volume versus pore width, C) Incremental Pore surface Area versus pore width and D) Volumes ratio of primary (i.e. 2 to 10 nm) and secondary pores (i.e. 10 nm to 100 nm) to the total pore volume for Pt/KB Std CL, Pt/VC Std CL, Pt/VC|Pt/KB CL, Pt/KB|Pt/VC and Blended Pt/KB:Pt/VC CL.

The total BET surface area (SA), total pore volume, volumes and surface area distributions in various pore regions of the CLs are summarized in Table 1. The BET_{total} surface area was 526 m^2/g_{carbon} for the Pt/KB Std CL and 72 m^2/g_{carbon} for the Pt/VC Std CL estimated in the partial pressure range of 0.05-0.30 P/P_0. The main difference in the BET_{total} SA for these cathode CLs is caused by small pores with diameters of less than 10 nm, largely present for KB-containing CLs but not for the Pt/VC Std CL. The BET surface area contributed from pores larger than 10 nm is about 14% for the Pt/KB Std CL and to 62% for the Pt/VC Std CL. The total pore volumes are 1.40 cm^3/g_{carbon} for the Pt/KB Std CL and 0.66 cm^3/g_{carbon} for the Pt/VC Std

CL. The volume of micropores ($V_{pore<2nm}$) was calculated as stated by Soboleva *et al.* [50] using the intercept of the t-plot with the ordinate , although in the case of the Pt/VC Std CL, this intercept is negative suggesting the absence of detectable micropores.

The Pt/VC|Pt/KB CL, Pt/KB|Pt/VC CL and the Blended Pt/KB:Pt/VC CL have comparable BET_{total} surface area and combination of micro- and meso-porous regions. Additionally, these multi-component CLs have porosity and surface area metrics that correlate very well with the stoichiometric amounts of each single component, compared to the Standard CLs described in the previous paragraph. The calculated $V_{pore\ total}$ are 1.13 cm^3/g_{carbon}, 0.91 cm^3/g_{carbon}, and 1.02 cm^3/g_{carbon}, respectively. The $V_{pore<2nm}$ calculated for the Pt/VC|Pt/KB CL, Pt/KB|Pt/VC CL and the Blended Pt/VC:Pt/KB CL are 0.0094 cm^3/g_{carbon}, 0.0073 cm^3/g_{carbon}, and 0.0126 cm^3/g_{carbon}, respectively.

These values of $V_{pore\ total}$ and $V_{pore<2nm}$ for the dual-layer CLs and the blended CL are lower than that of the Pt/KB Std CL, but substantially higher than that of the Pt/VC Std CL. This observation is not surprising and reflects the CL composition as these CLs contain about 25 wt.% less Pt/KB catalyst.

	Pt/KB Std CL	Pt/VC Std CL	Pt/VC|Pt/KB CL	Pt/KB|Pt/VC CL	Blended Pt/VC:Pt/KB CL
CL thickness (μm)	10.2	7.8	10.8	10.8	10.4
BET SA_{total} (m^2/g_{carbon})	566	72	391	326	380
$SA_{>2nm}$ (m^2/g_{carbon})	527	72	376	314	359
$SA_{<2nm}$ (m^2/g_{carbon})	39	-	15	12	21
$V_{pore,total}$ (cm^3/g_{carbon})	1.40	0.66	1.13	0.91	1.06
$V_{pore<2nm}$ (cm^3/g_{carbon})	0.0233	-	0.0094	0.0073	0.0126
Porosity %	61	43	56	51	54

Table 1. Microstructural characteristics of the Pt/KB Std CL, Pt/VC Std CL, Pt/VC|Pt/KB CL, Pt/KB|Pt/VC CL and Blended Pt/VC:Pt/KB CL determined from the N_2-adsorption isotherms.

Figure 3B and 3C show the incremental pore volume size distribution (PSD) and the incremental pore surface area distribution, respectively. All of the CLs have a comparable PSD ranging from 2 to 180 nm, with the most pore volume centered in the 45 nm pores for the CLs containing pure KB-based layers (Fig. 3B). Fig. 3B & 3C clearly show two distinctive PSD regions. A first region is in the range of pore widths of 2 to 10 nm, which is referred to as the primary pore region (essentially, the pores existing inside the grains of carbon composing the CL [59]). There is a second region in the range of pore widths of 10 nm to 100 nm, which is often referred to as the secondary pore region (essentially, the pores between the carbon grains composing the CL [59]). Soboleva *et al.*[50], Suzuki *et al.*[60] and Yu *et al.*[61] made comparable observations for cathode CLs manufactured using Pt/CB catalyst similar to those employed in this work. The ratio of primary pore and secondary pore volumes to the total pore volume is nearly identical for the Pt/VC|Pt/KB CL, Pt/KB|Pt/VC CL and the Blended Pt/KB:Pt/VC CL as shown in Fig. 3D. These CLs have slightly less secondary pores and slightly more primary pores than the Pt/KB standard CL, which was expected (they contain ¾ of the KB carbon of the Pt/KB standard CL, hence the smaller amount of primary pores).

While CL's pore structure is important for transporting of O_2 to, and H_2O away from, the Pt electrocatalyst, the CL's porosity is another important structural parameter that affects mass-transport. The CL's porosity was calculated according to Eq. 2 [60]:

$$\epsilon_{\mathrm{CL}}\,(\%) = V_{\mathrm{pore,total}}/(V_{\mathrm{pore,total}} + {}^{\alpha}/_{\rho_{\mathrm{ionomer}}} + {}^{1}/_{\rho_{\mathrm{carbon}}} + {}^{\beta}/_{\rho_{\mathrm{Pt}}}) \qquad [2]$$

where ϵ_{CL} is the CL porosity (%), $V_{\text{pore total}}$ is the total pore volume measured from the N_2-sorption porosimetry, α is the weight ratio of ionomer to carbon (i.e. 0.62), β is the weight ratio of Pt to carbon (i.e. 0.40) and ρ is the density (i.e. Pt = 21.45 g cm^{-3}, carbon = 1.9 g cm^{-3} and ionomer = 2 g cm^{-3})[46, 60, 62]. The porosities of the CLs studied in this work range from a high of 61% for the Pt/KB Std CL to a low of 43 % for the Pt/VC Std CL. The porosity of the Pt/VC|Pt/KB CL, Pt/KB|Pt/VC CL and the Blended

Pt/VC:Pt/KB CL are fairly comparable to each other. The porosity values measured here are within the normal range of CL porosities [2, 46, 60, 63].

3.3. Electrochemical Evaluation of Single Cells

The five different CLs have notable differences in electrochemical performance, particularly at 25% RH, as shown in the polarization curves in Figure 4. Fig. 4A & Fig. 4B compare the average polarization and power density curves measured at 100% and 25% RH, respectively, while Fig. 4C & Fig. 4D compare the average *iR*-corrected polarization curves and ohmic resistances of fuel cells with the five different cathodes at 100% and 25% RH, respectively.

There is almost no impact of the different cathodes at 0.80 V, where differences in current arise mainly from kinetic (i.e., charge-transfer) losses, distinct from the mass-transport or ohmic losses more prevalent at greater polarizations. For the PEMFCs containing the Pt/VC|Pt/KB CL, the Pt/KB|Pt/VC CL, and the Blended Pt/VC:Pt/KB CL the current densities are very similar to that of the PEMFC containing the Pt/KB Std CL. The somewhat improved performance of these PEMFCs in the kinetic portion of the polarization curve compared to the PEMFC including the Pt/VC Std CL is not surprising given their larger Pt ECSA, as demonstrated in Fig. S2. These results are summarized in Table 2.

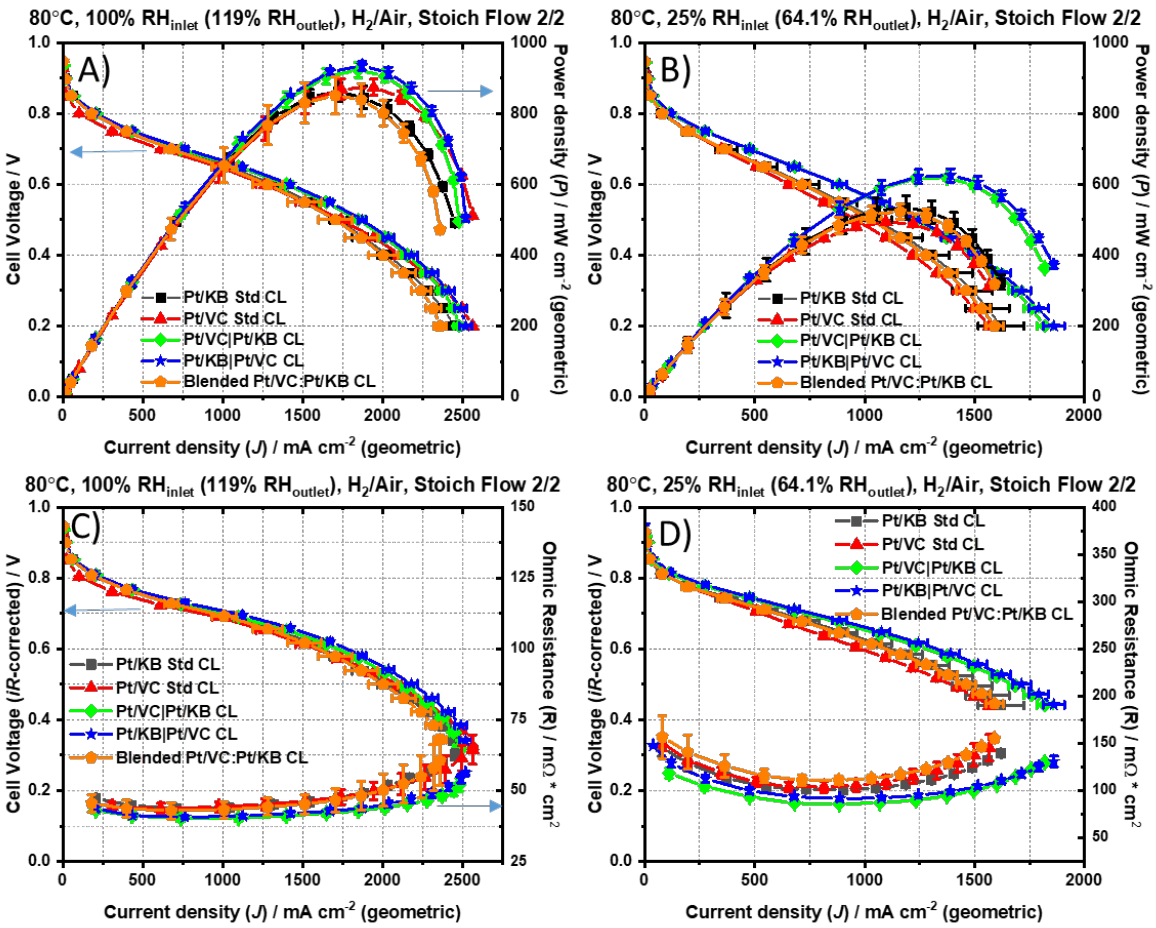

Figure 4. I-V polarization and power density curves recorded for five single cell PEMFCs containing either a Pt/KB Std CL, a Pt/VC Std CL, a Pt/VC|Pt/KB CL, a Pt/KB|Pt/VC CL or a Blended Pt/KB:Pt/VC CL at a cell temperature of 80 °C, ambient pressure, in H_2/air environment under stoichiometric flow of 2/2 at (A,C) 100% RH and (B, D) 25% RH. Fig.4C) and 4D) present the iR-corrected I-V polarization curves and ohmic resistances measured for the same single cell PEMFCs under the same operating conditions. The error bars correspond to the standard deviation for three individual polarization curve measurements performed for each PEMFC.

At lower cell voltages and higher current densities, where O_2, H^+ consumption and water production is higher, the PEMFCs with the dual-layer CLs exhibit marginally higher performance under "wet" (i.e. 100% RH) and significantly higher performance under"dry" (i.e. 25% RH) conditions compared to the Pt/KB Std CL, Pt/VC Std CL, or Blended Pt/VC:Pt/KB CL. These differences in performance are observed for the different CLs despite having similar Pt electrochemical surface areas (as shown in Fig. S2). At the operating

cell voltage of 0.50 V, the PEMFCs with dual-layer cathode CLs had a 26 % higher peak power density than the other PEMFCs under investigation.

	Current density @ 0.80 V (mA cm^{-2})		Current density @ 0.60 V (mA cm^{-2})		Peak Power density @ 0.50 V (mW cm^{-2})		Ohmic resistance @ 0.60 V (mΩ * cm^2)	
	100% RH	25% RH	100% RH	25 % RH	100% RH	25% RH	100% RH	25% RH
Pt/KB Std CL	205 ± 13	76 ± 9	1316 ± 26	732 ± 59	861 ± 27	534 ± 33	45 ± 1	101 ± 1
Pt/VC Std CL	101 ± 1	82 ± 3	1263 ± 55	656 ± 17	873 ± 27	493 ± 5	45 ± 1	103 ± 1
Pt/VC|Pt/KB CL	205 ± 6	111 ± 3	1397 ± 37	884 ± 4	934 ± 13	625 ± 6	41 ± 1	86 ± 1
Pt/KB|Pt/VC CL	201 ± 12	120 ± 7	1422 ± 4	886 ± 32	923 ± 21	625 ± 18	42 ± 1	92 ± 1
Blended Pt/VC:Pt/KB CL	180 ± 12	80 ± 12	1280 ± 93	715 ± 37	851 ± 53	523 ± 22	44 ± 1	111 ± 1

Table 2. Performance markers of the MEAs operated in similar conditions at 100 and 25% RH for different cathode CL configurations. Data extracted from the plots of Figure 4.

At lower RH (i.e. 25%) dual-layer cathode CLs have a greater impact on the cell performance. As show in Table 2, the peak power density of the PEMFCs containing the Pt/KB Std CL is 534 ± 33 mW cm^{-2} and 493 ± 5 mW cm^{-2} for Pt/VC Std CL, a decreases of about 43% compare to the peak power density measured at 100% RH for the same CLs. This decrease in peak power density is largely attributed to the decrease in proton activity that occurs in the CL at below 30% RH, which adversely affects the ORR [64]. When the RH is reduced from 100 to 25%, the PEMFCs with dual-layer CLs exhibit a substantially lower performance loss. When compared to the Pt/KB Std CL, Pt/VC Std CL, and Blended Pt/VC:Pt/KB CL, the Pt/VC|Pt/KB CL and Pt/KB|Pt/VC CL performed considerably better at this low RH situation.. For the dual-layer CLs, the current density measured at an operating cell voltage of 0.60 V and peak power density measured at a cell voltage of 0.50 V are about 26% higher and 21% higher at 25% RH compared to the PEMFC containing the containing the Pt/KB Std CL, the Pt/VC Std CL and the Blended Pt/VC:Pt/KB CK.

Counter to our original hypothesis, the direction of the porosity of the Pt/VC or the Pt/KB dual-layers relative to the Nafion® HP PEM does not have a major impact on the cell performance at either RH, and the performance is equivalent when the porosity either increases or decreases down the Z-axis. Figure 4 and Table 2 clearly shows that the location of the higher porosity CL (i.e. Pt/KB CL see Table 1) at the PEM interface or at the GDM/MPL interface has no impact on the overall cell performance. Only the presence of gradient in porosity distribution or the presence of interfaces within the CL seems to affect the MEA performance. This observation is surprising and the reasons for the enhanced performance independent of porosity gradient is worthy of future investigation. One tentative explanation could be that an interface inside the catalyst layer enhances performance independent of its position in the Z-axis, perhaps by aiding lateral X-Y mass transport and cell hydration. Future experiment will be required to determine the precious mechanism of this observed improvement. Another tentative explanation could be the density of each of the CL in the dual-layer cathode CL. Figure 2 and Table 4 clearly shows that the Pt/VC Std CL is thinner and less porous than the Pt/KB Std CL implying a denser CL for the former. Yi *et al.* [65, 66] recently reported the creation of a highly effective self-humidifying MEA by depositing a nano-sized dense structure (NSDS) layer onto a conventional CL, resulting in a dual-layer CL that promotes self-humidification. X-ray computed tomography was used to explore the mechanism for water retention, which revealed that the NSDS layer provides a very tortuous pore channel that considerably slows water transportation, increasing cell performance at low RH conditions.

iR-corrected I-V polarization curves, in which contribution from the bulk PEM resistance is removed, together with the ohmic resistances measured by the current-interrupt technique, are shown in Fig. 4C & 4D. The PEMFC comprising the dual-layer cathode CLs exhibited lower ohmic resistances in both wet and dry conditions. At 100% RH, the dual-layer cathodes have about 3 mΩ cm^2 less resistance than the standard and blended cathode electrodes. In dry conditions (i.e. 25%RH), the average ohmic resistances measured at 0.60 V are about 10-15 mΩ cm^2 less resistive for the dual-layer CLs vs. the standards and

blended cathode CLs. The *iR*-corrected polarization curves still exhibit major performance differences, indicating that additional sources of resistances for the PEMFC comprise Pt/KB Std CL, Pt/VC Std CL, and the Blended Pt/VC:Pt/KB CL are significant. Factors in addition to higher ohmic resistance (which is dominated by PEM hydration) are contributing to their lower performances compared to PEMFCs comprised of the dual-layer cathode CLs.

Figure 5 depicts the EIS results for the five different cathode CLs in fuel cells at 0.60 V and 100% RH or 25% RH. The left intercept on the X-axis in the high frequency domain of the EIS results in Fig. 5A & 5C is due to ohmic resistance (R_{ohm}), which comes mostly from the ionic resistance in the electrolyte and the CL. The difference between the low frequency intercept and the high frequency intercept on X-axis (i.e. the diameter of the spectra R_{total}) is, in first approximation, the sum of the effective charge-transfer resistances ($R_{ct,}$) and the mass-transport resistance (R_{mt}) [2, 10]. At each RH, the graph form is largely made up of two depressed semi-circles from the kinetic resistance and the mass-transport resistance for the ORR.

To determine the contributions to the impedance spectra from cathode kinetic and mass transport processes, the equivalent circuit model (ECM) proposed by Qiu *et al.* [36] was used, and the results are presented in Fig. 5B & 5D. At 100% RH no significant changes in the ohmic resistances (R_{ohmic}) are seen for all the PEMFCs, as shown in Fig. 5A, complementing our results by current-interrupt displayed in Fig. 4C. However, Fig. 5A clearly shows that the dual-layer PEMFCs comprising the Pt/VC|Pt/KB CL and the Pt/KB|Pt/VC CL have comparable R_{ct} and R_{mt} (i.e. 180 mΩ cm^2 and 200 mΩ cm^2, respectively) and both are lower than all the other PEMFC cathode CLs tested.

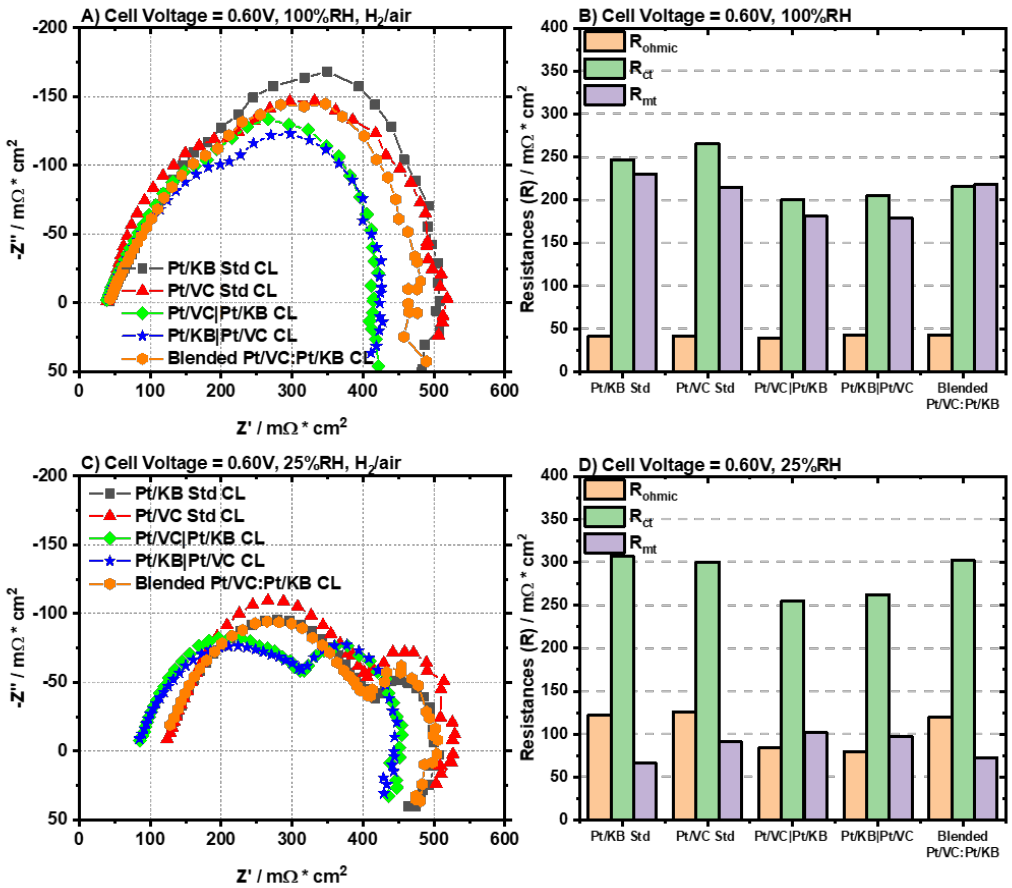

Figure 5. Electrochemical impedance spectra measured in situ while the PEMFC is operated is operated at cell voltage of 0.60 V, at cell temperature of 80°C, in H_2/air at A) 100%RH and C) 25%RH. Comparison of the sources of resistance obtained by fitting the EIS spectra with the ECM at B) 100% RH and D) 25% RH.

At 25%RH, shown in Fig. 5C & 5D, the dual-layer CLs with Pt/VC|Pt/KB CL and Pt/KB|Pt/VC CL exhibit reduced R_{ohmic} of 84 mΩ cm^2 and 80 mΩ cm^2 respectively, approximately 40 mΩ cm^2 lower than that of both the Pt/VC Std CL and Pt/KB Std CLs and the Blended Pt/VC:Pt/KB CL (~120 mΩ cm^2). We also observed the reduced R_{ct} values for the PEMFC comprised of the dual-layer CLs by a maximum of 17% (254 mΩ cm^2 for the Pt/KB|Pt/VC CL and 262 mΩ cm^2 for Pt/VC|Pt/KB CL, respectively) compared to that of both the Pt/VC Std and Pt/KB Std cathode CLs and the Blended Pt/VC:Pt/KB CL (~304 mΩ cm^2). These findings suggest that a dual-layer cathode CL hydrates the Nafion® HP PEM effectively and aids the ORR by providing enough water molecules for enhanced proton transport without sacrificing mass transport.

The higher activity of the dual-layer CLs is attributed to higher hydration levels (better retention of water at low RH conditions). While the proton activity of the ORR falls off below 30% RH in conventional fuel cells due to decreased hydration [64], the dual-layer cathode CL seem to provide a path for increasing the proton activity at low RH, resulting in maintained cell performance. To elucidate water with these structural changes in the cathode CL and to understand how the dual-layer cathode CLs act to maintain hydration without major reductions in oxygen transport, more research using Neutron imaging or X-ray tomography would be required.

4. Conclusions

When compared to a typical, homogenous CL created using a single type of supported catalyst, a dual-layer of Pt/C catalysts with varying porosities improves PEMFC performance. Surprisingly, the direction of the porosity of the Pt/VC or the Pt/KB dual-layers relative to the Nafion® HP PEM has no major impact on the cell performance, and the cell performance is similar when the porosity either increases or decreases down the Z-axis. Further, performance benefits grow in drier operating conditions (25% RH). The average porosity is also unimportant, as the Blended Pt/KB:Pt/VC cathode CLs with the same catalyst composition do not improve cell performance. These findings imply that buried interfaces, such as those between distinct layers in the dual-layer cathode CL, are significant, because they adsorb water and improve hydration.

The advantage provided by the dual-layer cathode design is seen not at lower current densities (kinetic region, approximately 0.80 V), but rather at more mass-transport constrained situations at cell operating voltages ≤ 0.60 V; it continues at all cell operation conditions, particularly at low RH conditions. At 25% RH , the improved current densities measured at an operating cell voltage of 0.60 V and peak power density at 0.50 V for the PEMFC containing the Pt/VC|Pt/KB cathode CL (i.e. 884 ± 5 mA cm^{-2} and

625 ± 6 mW cm^{-2}) and for the PEMFC containing the Pt/KB|Pt/VC cathode CL (i.e. 886 ± 33 mA cm^{-2} and 625 ± 18mW cm^{-2}) are about 20% higher compared to the PEMFC containing the containing the Pt/KB Std cathode CL and Std Pt/VC Std cathode CL. According to EIS analyses, the uniform I-V performance improvement in the PEMFC comprised of dual-layer cathode CLs can be attributed to lower ohmic, mass-transport, and kinetic resistances in the cathode compared to PEMFC comprised of a homogenous cathode CL design or a blended cathode CL design, which stems from the former's better retention of liquid water at low RH.

Acknowledgements

The authors would like to express their appreciation to the Office of Naval Research for its financial support of this effort.

5. References

[1] J.P. Owejan, J.E. Owejan, W. Gu, J. Electrochem. Soc., 160 (2013) F824-F833.
[2] Y. Garsany, R.W. Atkinson, M.B. Sassin, R.M.E. Hjelm, B.D. Gould, K.E. Swider-Lyons, J. Electrochem. Soc., 165 (2018) F381-F391.
[3] M. Chatenet, L. Dubau, N. Job, F. Maillard, Catal. Today, 156 (2010) 76-86.
[4] M.B. Sassin, Y. Garsany, B.D. Gould, K.E. Swider-Lyons, Anal. Chem., 89 (2017) 511-518.
[5] Z. Poltarzewski, P. Staiti, V. Alderucci, W. Wieczorek, N. Giordano, J. Electrochem. Soc., 139 (1992) 761.
[6] M. Uchida, Y. Aoyama, N. Eda, A. Ohta, J. Electrochem. Soc., 142 (1995) 4143.
[7] S. Sambandam, V. Ramani, Phys. Chem. Chem. Phys., 12 (2010) 6140-6149.
[8] C. Lei, D. Bessarabov, S. Ye, Z. Xie, S. Holdcroft, T. Navessin, J. Power Sources, 196 (2011) 6168-6176.
[9] Y.-C. Park, K. Kakinuma, H. Uchida, M. Watanabe, M. Uchida, J. Power Sources, 275 (2015) 384-391.
[10] Y. Garsany, R.W. Atkinson, B.D. Gould, K.E. Swider-Lyons, J. Power Sources, 408 (2018) 38-45.
[11] S. Shahgaldi, I. Alaefour, X. Li, Appl. Energy, 217 (2018) 295-302.
[12] K. Talukdar, P. Gazdzicki, K.A. Friedrich, J. Power Sources, 439 (2019) 227078.
[13] J. Zhao, X. He, L. Wang, J. Tian, C. Wan, C. Jiang, Int. J. Hydrog. Energy, 32 (2007) 380-384.
[14] A. Zlotorowicz, K. Jayasayee, P.I. Dahl, M.S. Thomassen, S. Kjelstrup, J. Power Sources, 287 (2015) 472-477.
[15] N. Job, S. Berthon-Fabry, M. Chatenet, J. Marie, M. Brigaudet, J.P. Pirard, Top. Catal., 52 (2009) 2117-2122.
[16] J. Marie, S. Berthon-Fabry, M. Chatenet, E. Chainet, R. Pirard, N. Cornet, P. Achard, J. Appl. Electrochem., 37 (2007) 147-153.

[17] J. Marie, R. Chenitz, M. Chatenet, S. Berthon-Fabry, N. Cornet, P. Achard, J. Power Sources, 190 (2009) 423-434.
[18] N. Zamel, J. Power Sources, 309 (2016) 141-159.
[19] A. Orfanidi, P.J. Rheinlander, N. Schulte, H.A. Gasteiger, J. Electrochem. Soc., 165 (2018) F1254-F1263.
[20] H. Yu, J.M. Roller, W.E. Mustain, R. Maric, J. Power Sources, 283 (2015) 84-94.
[21] S. Shukla, D. Stanier, M.S. Saha, J. Stumper, M. Secanell, J. Electrochem. Soc., 163 (2016) F677-F687.
[22] X. Peng, T. Omasta, W. Rigdon, W.E. Mustain, J. Electrochem. Soc., 163 (2016) E407-E413.
[23] R.M.E. Hjelm, C. Lafforgue, R.W. Atkinson, Y. Garsany, R.O. Stroman, M. Chatenet, K. Swider-Lyons, J. Electrochem. Soc., 166 (2019) F1218-F1228.
[24] L. Jabbour, C. Robin, F. Nandjou, R. Vincent, F. Micoud, J.P. Poirot-Crouvezier, J. d'Arbigny, M. Gerard, J. Power Sources, 299 (2015) 380-390.
[25] Y.G. Yoon, T.H. Yang, G.G. Park, W.Y. Lee, C.S. Kim, J. Power Sources, 118 (2003) 189-192.
[26] D.P. Wilkinson, J. St-Pierre, J. Power Sources, 113 (2003) 101-108.
[27] Z. Xie, T. Navessin, K. Shi, R. Chow, Q. Wang, D. Song, B. Andreaus, M. Eikerling, Z. Liu, S. Holdcroft, J. Electrochem. Soc., 152 (2005) A1171.
[28] M. Santis, S.A. Freunberger, A. Reiner, F.N. Büchi, Electrochim. Acta, 51 (2006) 5383-5393.
[29] H.-N. Su, S.-J. Liao, Y.-N. Wu, J. Power Sources, 195 (2010) 3477-3480.
[30] A.D. Taylor, E.Y. Kim, V.P. Humes, J. Kizuka, L.T. Thompson, J. Power Sources, 171 (2007) 101-106.
[31] M. Prasanna, E.A. Cho, H.J. Kim, I.H. Oh, T.H. Lim, S.A. Hong, J. Power Sources, 166 (2007) 53-58.
[32] K.H. Kim, H.J. Kim, K.Y. Lee, J.H. Jang, S.Y. Lee, E. Cho, I.H. Oh, T.H. Lim, Int. J. Hydrog. Energy, 33 (2008) 2783-2789.
[33] M. Srinivasarao, D. Bhattacharyya, R. Rengaswamy, S. Narasimhan, Int. J. Hydrog. Energy, 35 (2010) 6356-6365.
[34] Y. Tabe, M. Nishino, H. Takamatsu, T. Chikahisa, J. Electrochem. Soc., 158 (2011) B1246-B1254.
[35] H. Matsuda, K. Fushinobu, A. Ohma, K. Okazaki, J. Therm. Sci. Technol., 6 (2011) 154-163.
[36] Y. Qiu, H. Zhang, H. Zhong, F. Zhang, Int. J. Hydrog. Energy, 38 (2013) 5836-5844.
[37] G. Kim, K. Eom, M. Kim, S.J. Yoo, J.H. Jang, H.-J. Kim, E. Cho, ACS Appl. Mater. Interfaces, 7 (2015) 27581-27585.
[38] H. Liang, R. Xu, K. Chen, C. Shen, S. Yin, RSC Adv., 6 (2016) 1333-1338.
[39] G.-Y. Chen, C. Wang, Y.-J. Lei, J. Zhang, Z. Mao, Z.-Q. Mao, J.-W. Guo, J. Li, M. Ouyang, Int. J. Hydrog. Energy, 42 (2017) 29960-29965.
[40] L. Ye, Y. Gao, S. Zhu, J. Zheng, P. Li, J.P. Zheng, Int. J. Hydrog. Energy, 42 (2017) 7241-7245.
[41] G. Wang, L. Zou, Q. Huang, Z. Zou, H. Yang, J. Mater. Chem. A, 7 (2019) 9447-9477.
[42] L. Xing, W. Shi, H. Su, Q. Xu, P.K. Das, B. Mao, K. Scott, Energy, 177 (2019) 445-464.
[43] S. Shahgaldi, A. Ozden, X. Li, F. Hamdullahpur, Energy Convers. Manag., 171 (2018) 1476-1486.
[44] M. Eikerling, J. Electrochem. Soc., 153 (2006) E58-E70.
[45] Q. Wang, M. Eikerling, D. Song, Z. Liu, J. Electroanal. Chem., 573 (2004) 61-69.
[46] M.B. Sassin, Y. Garsany, R.W. Atkinson, R.M.E. Hjelm, K.E. Swider-Lyons, Int. J. Hydrog. Energy, 44 (2019) 16944-16955.
[47] J. Speder, A. Zana, M. Arenz, Catal. Today, 262 (2016) 82-89.
[48] J. Yu, M.N. Islam, T. Matsuura, M. Tamano, Y. Hayashi, M. Hori, Electrochem. Solid-State Lett., 8 (2005) A320.
[49] Y. Garsany, R.W. Atkinson III, B.D. Gould, 2020, Multi-Interface Membrane Electrode Assembly, US Provisional Application No. 63/039,762.
[50] T. Soboleva, X. Zhao, K. Malek, Z. Xie, T. Navessin, S. Holdcroft, ACS Appl Mater Interfaces, 2 (2010) 375-384.

[51] Y. Garsany, C.H. Bancroft, R.W. Atkinson, K. Bethune, B.D. Gould, K.E. Swider-Lyons, Molecules, 25 (2020).
[52] R.W. Atkinson, Y. Garsany, B.D. Gould, K.E. Swider-Lyons, I.V. Zenyuk, ACS Appl. Energy Mater., 1 (2018) 191-201.
[53] M.B. Sassin, Y. Garsany, B.D. Gould, K. Swider-Lyons, J. Electrochem. Soc., 163 (2016) F808-F815.
[54] Y.C. Park, H. Tokiwa, K. Kakinuma, M. Watanabe, M. Uchida, J. Power Sources, 315 (2016) 179-191.
[55] V. Yarlagadda, M.K. Carpenter, T.E. Moylan, R.S. Kukreja, R. Koestner, W. Gu, L. Thompson, A. Kongkanand, ACS Energy Lett., 3 (2018) 618-621.
[56] T. Soboleva, K. Malek, Z. Xie, T. Navessin, S. Holdcroft, ACS Appl Mater Interfaces, 3 (2011) 1827-1837.
[57] N. Krishnankutty, M.A. Vannice, Chem. Mater., 7 (1995) 754-763.
[58] K.S.W. Sing, D.H. Everett, R.A.W. Haul, L. Moscou, R.A. Pierotti, J. Rouquerol, T. Siemieniewska, Pure Appl Chem, 57 (1985) 603-619.
[59] M. Uchida, Y. Fukuoka, Y. Sugawara, N. Eda, A. Ohta, J. Electrochem. Soc., 143 (1996) 2245-2252.
[60] T. Suzuki, S. Tsushima, S. Hirai, Int. J. Hydrog. Energy, 36 (2011) 12361-12369.
[61] H.R. Yu, J.M. Roller, W.E. Mustain, R. Maric, J Power Sources, 283 (2015) 84-94.
[62] E. Hoffmann, S. Zhang, M. Thoma, C. Damm, W. Peukert, Particuology, 44 (2019) 7-21.
[63] S.-D. Yim, Y.-J. Sohn, S.-H. Park, Y.-G. Yoon, G.-G. Park, T.-H. Yang, C.-S. Kim, Electrochim. Acta, 56 (2011) 9064-9073.
[64] K.C. Neyerlin, H.A. Gasteiger, C.K. Mittelsteadt, J. Jorne, W.B. Gu, J. Electrochem. Soc., 152 (2005) A1073-A1080.
[65] C.Y. Jung, S.K. Kim, S.J. Lee, S.C. Yi, Electrochim. Acta, 211 (2016) 142-147.
[66] B.S. Koh, J.H. Yoo, E.K. Jang, V.R. Jothi, C.Y. Jung, S.C. Yi, Electrochem. commun., 93 (2018) 76-80.